International Journal of Nanomedicine

Dovepress
Taylor & Francis Group

Open Access Full Text Article

ORIGINAL RESEARCH

Gold/Prussian Blue-Based Nanocomposites with Dual Nanozyme Activities Exert a Synergistic Effect of Starvation Therapy and Sonodynamic Therapy in the Treatment of Liver Cancer

Shengnan Huang[1,2,*], Chengzhi Song[3,*], Tengyue Zhao[4,*], Yefei Yang[4], Zhiwei Yao[4], Shaofeng Duan[5], Wanyi Chen[6], Lixian Li[6], Xiaogang Hu[6], Chunming Li[6], Yurong Hu[4]

[1]Academy of Chinese Medical Sciences, Henan University of Chinese Medicine, Zhengzhou, 450046, People's Republic of China; [2]Collaborative Innovation Center of Research and Development on the Whole Industry Chain of Yu-Yao, Henan Province, Henan University of Chinese Medicine, Zhengzhou, 450046, People's Republic of China; [3]Center for Quantitative Biology, Peking University, Beijing, 100871, People's Republic of China; [4]School of Pharmaceutical Sciences, Key Laboratory of Targeting Therapy and Diagnosis for Critical Diseases, Zhengzhou University, Zhengzhou, 450001, People's Republic of China; [5]School of Pharmaceutical Sciences, Henan University, Zhengzhou, 450046, People's Republic of China; [6]Department of Pharmacy, Chongqing University Cancer Hospital, Chongqing, 400030, People's Republic of China

*These authors contributed equally to this work

Correspondence: Chunming Li; Yurong Hu, Email lchm@cqu.edu.cn; huyr@zzu.edu.cn

Purpose: This study aimed to develop a composite nanozyme system (Au/PB-Ce6-HA) based on gold nanoparticles (AuNPs) and Prussian blue nanoparticles (PBNPs) to combat tumor hypoxia and insufficient endogenous hydrogen peroxide (H_2O_2) deficiency, thus enhancing the efficacy of sonodynamic therapy (SDT) and starvation therapy for liver cancer.

Methods: The Au/PB-Ce6-HA system was constructed by in situ embedding AuNPs on PBNPs, loading the sonosensitizer Chlorin e6 (Ce6), and surface-coating with thiolated hyaluronic acid (HA-SH). The system was evaluated both in vitro and in vivo to assess its ability to catalyze glucose to generate H_2O_2, decompose H_2O_2 to produce oxygen, and generate highly toxic reactive oxygen species (ROS) under ultrasound irradiation.

Results: The Au/PB-Ce6-HA nanozymes demonstrated high catalytic activity, thus significantly improving SDT and starvation therapy. Specifically, the system effectively deprived tumors of their energy supply by generating H_2O_2, while simultaneously producing oxygen to enhance cytotoxic ROS generation under ultrasound irradiation. Both in vivo and in vitro studies further demonstrated a synergistic effect in inhibiting tumor growth while enhancing therapeutic efficacy.

Conclusion: An intelligent composite nanomaterial was successfully developed, combining starvation therapy and sonodynamic therapy to significantly enhance the treatment of liver cancer. The Au/PB-Ce6-HA nanozyme system demonstrated excellent synergy in both in vitro and in vivo settings, offering a promising strategy for cancer therapy.

Keywords: gold nanoparticles, Prussian blue nanoparticles, composite nanozyme, sonodynamic therapy, starvation therapy

Introduction

Cancer is one of the most threatening diseases to human health. The low overall survival rate and poor prognosis of cancer patients remain a huge challenge, particularly for hepatocellular carcinoma (HCC) which remains the most common type among primary liver cancers.[1] HCC presents unique clinical challenges including frequent late-stage diagnosis due to asymptomatic progression, with a substantial majority of patients presenting at advanced stages when curative options are limited.[2] The hypoxic tumor microenvironment characteristic of HCC not only promotes angiogenesis and metastasis but also severely compromises oxygen-dependent therapies.[3,4] Furthermore, HCC cells exhibit much higher glucose uptake than normal hepatocytes due to the Warburg effect, creating a metabolic vulnerability that current treatments fail to selectively

Received: 19 September 2024
Accepted: 18 July 2025
Published: 1 September 2025

exploit.[5] Conventional surgery, radiotherapy, and chemotherapy are further hindered by significant drug resistance, harmful side effects, and inherent shortcomings such as a high risk of recurrence, which often brings great pain to patients.[6,7] In recent years, with the development of nanotechnology, some minimally invasive or non-invasive treatment methods have been developed for cancer treatment.[8,9] In photothermal therapy (PTT), light is transformed into heat upon near-infrared (NIR) light excitation to inhibit tumor tissues by using photothermal conversion agents.[10,11] In photodynamic therapy (PDT), specialized light is utilized to activate photosensitizers to convert oxygen (O_2) molecules into ROS, such as singlet oxygen ($^1O_2$) and hydroxyl radicals (•OH).[12,13] Consequently, cell damage occurs through peroxidation of the cell membrane, disruption of DNA/proteins, and impairment of signal functions/gene transcription.[14–16] However, it is worth noting that PDT faces a significant limitation due to the restricted depth of light penetration in tissues, which diminishes its efficacy in treating tumors located deep within the body.[13,17] Ultrasound (US), as a mechanical wave with a relatively low tissue attenuation coefficient, can penetrate tissues deeper than 10 centimeters.[18] Extensive studies, such as ultrasound imaging and high-intensity focused ultrasound (HIFU), have been conducted in the clinical field exploring the use of US for the diagnosis and treatment of cancers.[19,20] Sonodynamic therapy (SDT) originates from PDT, and both require O_2 and sensitizers.[21,22] Chlorin e6 (Ce6), the sonosensitizer employed in this study, features a porphyrin-derived macrocyclic structure with three carboxyl groups and a conjugated dihydroporphyrin ring system. This unique architecture enables efficient energy transfer from ultrasound to molecular oxygen, generating cytotoxic singlet oxygen ($^1O_2$) through type II photodynamic pathways. The primary difference between these two techniques lies in the energy source used to activate the sensitizer, with SDT using US while PDT utilizing light.[23–25]

Since ultrasonic waves penetrate over 10 centimeters - significantly deeper than optical modalities - SDT activates sonosensitizers in deep tumors. However, conventional SDT remains constrained by tumor hypoxia and endogenous H_2O_2 deficiency.[26,27]

The selection of Au, PB, and Ce6 for our nanocomposite design addresses these limitations through complementary functionalities: Prussian blue nanoparticles (PBNPs) provide catalase-mimetic activity within their porous framework, enabling endogenous H_2O_2 decomposition to alleviate hypoxia while serving as drug carriers.[28] Gold nanoparticles (AuNPs) offer glucose oxidase-like activity to starve tumor cells and generate H_2O_2, with surface plasmon resonance properties enhancing Ce6's sonosensitization efficiency.[29] Ce6 was chosen for its near-infrared absorption, deep-tissue penetration capability, and proven clinical safety profile in photodynamic therapies.[30] This synergistic combination creates a self-amplifying therapeutic cascade specifically engineered for hepatocellular carcinoma's unique microenvironment: AuNPs deplete glucose to cut off energy supply while generating H_2O_2; PBNPs convert H_2O_2 to oxygen; Ce6 transforms oxygen into tumor-killing ROS under ultrasound - all within an integrated platform exploiting the high H_2O_2 content characteristic of liver tumors.

As depicted in Scheme 1A, in this study, AuNPs were initially deposited onto the surface of PBNPs to obtain Au/PB NPs. As a composite nanozyme, Au/PB NPs not only exhibited catalytic activity but also efficiently loaded the sonosensitizer Ce6.[31–34] Subsequently, we modified the Au/PB NPs with thiolated hyaluronic acid (HA-SH) as a targeting and blocking agent through gold-sulfur bonding. Ultimately, a dual nanozyme cascade catalytic delivery system, Au/PB-Ce6-HA NPs, was successfully developed.

As illustrated in Scheme 1B, Au/PB-Ce6-HA NPs can achieve efficient accumulation in tumor tissues through the EPR effect and HA-mediated active targeting. These nanoparticles can be endocytosed by tumor cells subsequently. The degradation of HA on the surface of Au/PB-Ce6-HA NPs can expose Au/PB NPs while simultaneously releasing the sonosensitizer Ce6. Notably, AuNPs, as a nanozyme mimicking glucose oxidase (GOx), can specifically catalyze the oxidation of glucose to glucuronic acid and H_2O_2, thereby cutting off the energy supply of the tumor cell. Moreover, the generated H_2O_2, as well as the endogenous H_2O_2 within the tumor, can then be catalyzed by the PBNPs exhibiting catalase (CAT) activity to produce O_2. Under ultrasound excitation, the generated O_2 can be converted into ROS by the sonosensitizer Ce6 to realize the combination of SDT and starvation therapy, thereby significantly enhancing the therapeutic effect on deep-seated tumors.

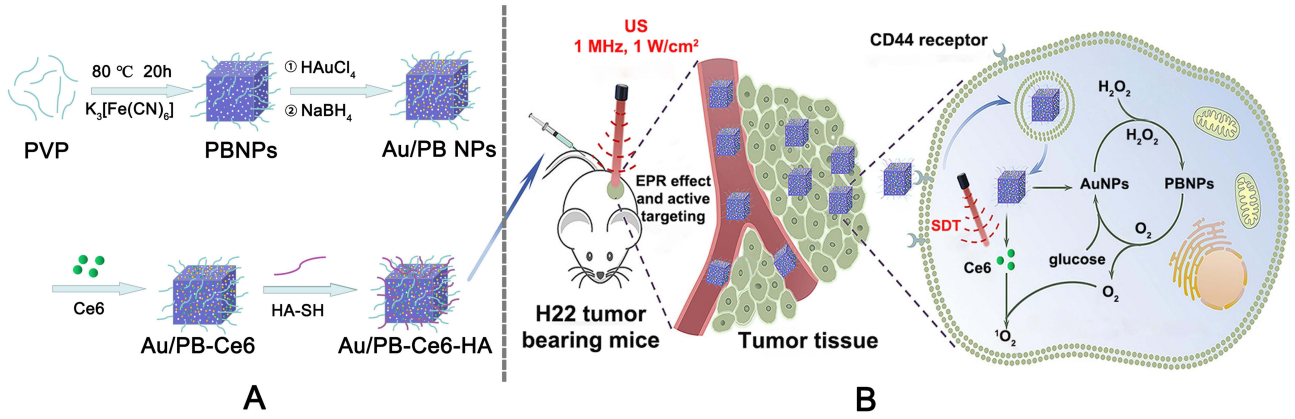

Scheme 1 Schematic illustration of the construction of the Au/PB-Ce6-HA cascade catalytic delivery system (**A**) and the mechanism for the combined SDT/starvation in cancer treatment (**B**).

Materials and Methods

Materials

Potassium ferricyanide ($K_3[Fe(CN)_6]$) was obtained from Tianjin Dingshengxin Chemical Co., Ltd, PR China. Hyaluronic acid (HA, MW = 8032 Da) was purchased from Bloomage Biotechnology Co., Ltd. (Jinan, PR China). Hydrogen tetrachloroaurate ($HAuCl_4 \cdot 4H_2O$) and hydrogen peroxide (H_2O_2) were obtained from Sinopharm Chemical Reagent Co., Ltd. (Shanghai, PR China). Polyvinylpyrrolidone (PVP) K30, NHS, EDC, and 2′,7′-dichlorodihydrofluorescein diacetate (DCFH-DA) were purchased from Aladdin Chemistry Co. (Shanghai, PR China). Sodium borohydride ($NaBH_4$), 4′,6-Diamidino-2-phenylindole (DAPI) and 3-(4,5-Dimethylthiazol-2-yl)-2,5-diphenyltetrazolium bromide (MTT) were purchased from Sigma-Aldrich (Shanghai, PR China). Chlorin e6 (Ce6) was obtained from Hunan Huateng Pharmaceutical Co., PR China.

All chemicals were of analytical quality and utilized without further purification. In all experiments, Milli-Q water was supplied by the Milli-Q system (resistivity 18.2 MΩ·cm at 25 °C).

Instruments

The particle size was measured by the Zetasizer Nano ZS90 (Malvern, U.K). A UV-Vis spectrophotometer (Shimadzu, Japan) was employed to record the UV-Vis absorption spectra of the samples. XPS spectra were analyzed by Thermo Fisher Scientific ESCALAB 250Xi Spectrometer Electron Spectroscopy (USA). Fluorescence imaging was conducted using an Eclipse 80i Fluorescence Microscope (Nikon, Japan). The flow cytometry data was obtained by the BD Accuri C6 instrument (BD Biosciences, USA). The Chattanooga 2776 Ultrasound Therapy Apparatus was produced by American DJO Co. Optical density (OD) measurements were performed at 490 nm using a Synergy H1 microplate reader (Bio-Teck, USA). The mice's fluorescence signal distribution was observed using the In-Vivo MS FX PRO fluorescent imaging system (Bruker, USA).

Preparation of PBNPs

PBNPs were fabricated according to the reported procedure with some modifications. 5 g of PVP and 685 mg of $K_3[Fe(CN)_6]$ were dissolved into 2 M of HCl solution (40 mL) under magnetic stirring for 0.5 h. The clear solution was then placed into a reaction kettle and heated at 80 °C for 20 h. After the reaction solution was cooled to room temperature, a precipitates were obtained by centrifugation and washed with acetone and ultrapure water. Eventually, PB nanoparticles coated with PVP were acquired through vacuum drying.

Preparation of Au/PB NPs

Au/PB NPs were prepared by growing AuNPs in situ on the surface of PBNPs. Briefly, 12 mg PBNPs were dispersed in ultrapure water to prepare a 0.5 $mg \cdot mL^{-1}$ PB solution, then 500 μL of $HAuCl_4$ (8 $mg \cdot mL^{-1}$) solution was added. The

https://doi.org/10.2147/IJN.S490343

resultant mixture was reacted for 30 seconds under magnetic stirring, followed by the addition of 240 μL of freshly prepared $NaBH_4$ solution (3.5 mg·mL^{-1}). Next, the mixture solution was centrifuged at 9,000 rpm for 20 min to obtain a precipitate which was washed with ultrapure water to afford the desired product, Au/PB NPs. The final particles were re-dispersed in ultrapure water and stored at 4 °C.

Preparation of Au/PB-Ce6-HA NPs

A quantity of 2 mg of Ce6 was dissolved in DMSO, and then the resulting solution was introduced into a solution of Au/PB NPs (4 mL, 0.5 mg·mL^{-1}). The resultant mixture was stirred for 24 h. After centrifugation and washing, the synthesized Au/PB-Ce6 NPs were isolated and dispersed into ultrapure water for further use. To enhance and confirm the mechanism of biocompatibility and targeting, the surface of the Au/PB-Ce6 NPs was modified using HA-SH, which relies on the robust Au-S bond. Briefly, HA-SH (20 mg) was added into Au/PB-Ce6 NPs solution (1 mL, 1.5 mg·mL^{-1}), and then the mixture was stirred overnight in an argon atmosphere at room temperature.

After centrifugation and washing, the obtained Au/PB-Ce6-HA NPs were isolated and dispersed into water for further use. A Tecnai 20 transmission electron microscope (FEI, USA) was used to image samples. A similar method was used to modify Au/PB NPs and PB-Ce6 NPs to provide Au/PB-HA NPs and PB-Ce6-HA NPs. The drug loading efficiency (the weight of incorporated Ce6 divided by the weight of Ce6-loaded nanoparticles) was calculated.

Characterization of Hydrodynamic Size and Zeta Potential

Appropriate aliquots of purified PBNPs, Au/PBNPs, Au/PB-Ce6, and Au/PB-Ce6-HA nanoparticles were dispersed in 2 mL deionized water and homogenized via ultrasonication. The hydrodynamic diameter of each sample was determined using dynamic light scattering (DLS) measurements with a nanoparticle size analyzer. Subsequently, zeta potential values were acquired in a dedicated electrophoretic cell. All measurements were performed in triplicate at 25°C, and results are reported as mean ± standard deviation.

Surface Area and Porosity Analysis

Nitrogen adsorption-desorption isotherms were measured at 77 K (−196°C) using a fully automated surface area and porosity analyzer (ASAP 2460, Version 3.01; Micromeritics Instrument Corp., USA). Brunauer-Emmett-Teller (BET) surface area and Barrett-Joyner-Halenda (BJH) pore size distribution were determined from the isotherms using the instrument's native software - critical parameters for evaluating nanocarrier drug-loading capacity. Before analysis, ~300 mg of freeze-dried PBNPs underwent vacuum degassing at 190°C for 6 hours.

Development of Ce6 Quantification Method

A stock solution of Ce6 was prepared under light-protected conditions by dissolving 5.0 mg of Ce6 powder in dimethyl sulfoxide (DMSO) within a 10-mL volumetric flask, followed by dilution to volume at room temperature to achieve 0.5 mg·mL^{-1} concentration. The solution was stored at 4°C. To determine the optimal detection wavelength, aliquots of the stock solution were diluted with DMSO:H_2O (1:1, v/v) and scanned from 300 to 800 nm using a UV-2700 spectrophotometer (Shimadzu). The characteristic absorption peak was identified from the spectrum. For calibration, serial dilutions (20, 40, 80, 120, 160, and 200 μL) of the stock solution were prepared in DMSO:H_2O (1:1, v/v) to yield standard solutions of 1, 2, 4, 6, 8, and 10 μg·mL^{-1}. Absorbance measurements were performed at the identified λ_{max} against solvent blanks.

Drug Release Behavior Assessment

The release kinetics of Ce6 from Au/PB-Ce6-HA NPs were evaluated under physiologically simulated conditions to assess pH and hyaluronidase effects. Four experimental groups were established: Group a (PBS, pH 7.4, blood simulation), Group b (0.1 M acetate buffer, pH 5.5, tumor microenvironment simulation), Group c (0.1 M acetate buffer, pH 4.5, lysosomal simulation), and Group d (pH 4.5 buffer + 150 U·mL^{-1} hyaluronidase, Sigma-Aldrich).

For release testing, 1.0 mL aliquots of Au/PB-Ce6-HA NPs suspension were loaded into dialysis bags (MWCO 7 kDa, Spectrum Labs) containing a 2.0 mL release medium. Each bag was immersed in a 15.0 mL external release medium within 50-mL centrifuge tubes and incubated at 37°C with orbital shaking at 150 rpm. At predetermined intervals (1, 2, 4, 6, 8, 12, and

24 h), 1.5 mL external medium was collected and immediately replaced with pre-equilibrated fresh medium maintained at 37°C. Collected samples were centrifuged at 9,000 rpm for 20 min to remove particulate contaminants. Ce6 concentration in supernatants was determined spectrophotometrically, and the cumulative release percentage was calculated according to the formula:

$$\text{Cumulative release } (\%) = \left(C_n V_t + \sum_{i=1}^{n-1} C_i \times V_s\right) / M_T \times 100\%$$

Where C_n is the drug concentration at time t_n, V_t is the total release medium volume, C_i is the concentration at prior sampling time t_i, V_s is the sample volume withdrawn per interval, and M_T is the total drug mass loaded in nanoparticles.

Detection of $^1O_2$

1,3-Diphenylisobenzofuran (DPBF) is a fluorescent probe for $^1O_2$. When $^1O_2$ is present in the system, DPBF undergoes a specific reaction with it, causing a decrease in the intensity of its characteristic absorption peak at 405 nm. By monitoring changes in the absorbance of DPBF at this wavelength, the ability of Ce6 to generate $^1O_2$ under ultrasound excitation can be indirectly evaluated. Ultrasound parameters of 1 MHz and 1 $W \cdot cm^{-2}$ were used to irradiate the experimental group (containing Ce6+DPBF) and the control group (containing only DPBF). Absorbance was measured at time points of 0, 30, 60, 120, 180, 240, 300, 360, 420, 480, and 540 s. Data from the experimental group were corrected using background signals from the control group, and ultraviolet-visible absorption spectra were plotted. Subsequently, Ce6, Au/PB-Ce6-HA and Au/PB-Ce6-HA+H_2O_2 (with the same Ce6 concentration) were mixed with DPBF solution, and the absorbance of the solution was detected after being irradiated with ultrasound (1 MHz, 1$W \cdot cm^{-2}$) for 4 min.

Detection of Enzyme Activity

Catalase-Like Activity

The catalase-like activity was assessed by monitoring H_2O_2 decomposition at 240 nm (UV-2700 spectrophotometer). H_2O_2 decomposition was monitored at 240 nm (λ_{max} for H_2O_2) as per established protocols. A standard curve was first established using H_2O_2 solutions (10–60 mM, pH 6.8) to ensure quantitative accuracy. H_2O_2 decomposition experiments were performed by adding 1 mL of catalase solution (10 $\mu g \cdot mL^{-1}$), PBNPs (100 $\mu g \cdot mL^{-1}$), Au/PB NPs (100 $\mu g \cdot mL^{-1}$), and Au/PB-HA (100 $\mu g \cdot mL^{-1}$), respectively, to 1 mL of H_2O_2 solution (30 mM, pH 6.8). Critically, the catalase-mediated reaction $2H_2O_2 \rightarrow O_2 + 2H_2O$ ensures that H_2O_2 consumption directly correlates with oxygen production. Absorbance decay at 240 nm was recorded every 20 min for 2 h, with the relative activity calculation explicitly representing oxygen generation capacity - a key therapeutic mechanism validated by enhanced ROS under ultrasound.

Glucose Oxidase-Like Activity

In the presence of O_2, glucose oxidase (GOx) can facilitate the oxidation of glucose into gluconic acid and H_2O_2. GOx, AuNPs, and Au/PB NPs solutions were added to 10 $mg \cdot mL^{-1}$ glucose solution respectively. The enzymatic reaction intrinsically links glucose consumption to H_2O_2 production. Residual glucose was quantified at specified intervals (0–180 min) using a blood glucose meter, whose detection principle relies on H_2O_2-dependent electrochemical oxidation, thus providing direct evidence of H_2O_2 generation.

Cell Culture

Under a 5% CO_2 atmosphere, the HepG2 cell line, which was obtained from the Shanghai Cell Bank of the Chinese Academy of Sciences (CAS, Shanghai, China), was cultivated at 37 °C in RPMI-1640 medium supplemented with 10% fetal bovine serum (FBS), 100 $U \cdot mL^{-1}$ penicillin, and 100 $\mu g \cdot mL^{-1}$ streptomycin.

In Vitro Cellular Observation by Confocal Laser Scanning Microscopy (CLSM) and Flow Cytometry Analysis

HepG2 cells in the logarithmic growth phase were seeded onto glass coverslips in a 6-well plate covered with sterile coverslips at a density of 1×10^5 cells per well. When the cell confluence reached around 70%-80%, the

culture medium was substituted with 1 mL of new medium containing free Ce6, Au/PB-Ce6, and Au/PB-Ce6-HA, respectively (Ce6: 10 μg·mL^{-1}). After incubation at 37 °C for durations of 0.5, 1, 2, 4 and 6 h, respectively, the medium used for culturing was removed. After being washed with PBS, the cells were treated with 4% (w/v) paraformaldehyde for 15 min and subsequently stained with DAPI for another 15 min. The cellular fluorescence signals were detected and images were captured using an Eclipse 80i fluorescence microscope (Nikon, Japan).

For flow cytometry quantitative analysis, HepG2 cells were seeded into six-well plates at a density of 1×10^5 cells per plate. Once the cell confluence reached around 70%-80%, the culture medium was substituted with 1 mL of fresh medium that contained free Ce6, Au/PB-Ce6, Au/PB-Ce6-HA (Ce6: 10 μg·mL^{-1}). Then, they were cultured for 4 h. After cell digestion, the cellular uptake data of each group was obtained by a BD Accuri C6 flow cytometer (BD Biosciences, USA).

In Vitro Evaluation of Cytotoxicity

HepG2 cells were cultured in 96-well plates with a density of 8000 cells per well using RPMI-1640 medium supplemented with 10% FBS. After incubation with different concentrations of PBNPs, Au/PB NPs or Au/PB-HA NPs, respectively, for 24 h, the cellular toxicity was evaluated using the standard protocol of MTT assay. Briefly, 100 μL of MTT solution (1 mg·mL^{-1}) was introduced into each well and incubated at 37 °C for 4 h. Following the careful removal of the medium, cells were treated with 100 μL of DMSO and pipetted up and down to dissolve crystals. Using a Synergy H1 microplate reader (Bio-Tek, USA), the optical density (OD) was quantified at 490 nm for each well. To investigate the effect of Ce6 or Au/PB-Ce6-HA on cell viability, cells were cultured as described above and treated with different concentrations of Ce6 or Au/PB-Ce6-HA. Following a 4-hour incubation period, the cells were rinsed and separated into two categories: one group was subjected to US irradiation (1 MHz, 1 W·cm^{-2}, 1 min), while the other group remained without any US exposure, serving as the control. Afterward, the cells were incubated at 37 °C overnight. The relative cell viability was determined by applying the subsequent formula: Relative cell viability = $OD_{sample}/OD_{control} \times 100\%$. Here, $OD_{control}$ and OD_{sample} denote the optical density (OD) of wells containing cells treated with culture medium and nanoagents, respectively. The average of each value was calculated based on three separate experiments.

In Vitro Intracellular ROS Detection

Six groups (blank cells treated with PBS as control, Ce6, Au/PB-Ce6-HA, PBS+US, Ce6+US, Au/PB-Ce6-HA +US) were set to compare the ROS generation capability in vitro. Similar to cellular uptake as observed by fluorescence microscope, cells were co-cultured with different nanoagents for 4 h. Then, 1 mL of DCFH-DA probe was added to each well. The US group was then exposed to US irradiation (1 MHz, 1 W·cm^{-2}, 1 min) in a dark environment and incubated for an additional 30 min. Afterward, the cells were rinsed with PBS 3 times and examined using an Eclipse 80i fluorescence microscope (Nikon, Japan). For semi-quantitative analysis, DCF fluorescence intensity was quantified from 5 random fields/group using ImageJ by measuring mean gray values.

Animals Model Establishment

Female Kunming (KM) mice (6 weeks old, 20 ± 2 g) were obtained from SPF Biotechnology Co., Ltd. (Beijing, China). All procedures were conducted following the "Laboratory Animal - Guideline for Ethical Review of Animal Welfare" (China) and the "Experimental Animal Management Methods of Henan Province", with approval from the Laboratory Animal Ethics Committee of Zhengzhou University. For tumor induction, cryopreserved H22 cells were resuscitated and injected intraperitoneally into KM mice. After 5–7 days, when the abdomen of mice appeared obviously swelling, the ascites were extracted, centrifuged and washed 3 times using PBS. The final cell concentration was adjusted to 1×10^7 cells mL^{-1}. Subsequently, 200 μL of suspended cells were injected subcutaneously into the right forelimb of each KM mouse.

In Vivo Fluorescence Distribution

When the tumor volume reached about 100 mm^3, free Ce6, Au/PB-Ce6 or Au/PB-Ce6-HA was intravenously injected into H22 tumor-bearing mice for in vivo imaging. Given that Ce6 inherently exhibits fluorescence, there is no need for

additional fluorescent dyes for labeling. After 4, 8, 12, and 24 h, the In-Vivo MS FX PRO fluorescent imaging system (Bruker, USA) was used to observe the fluorescence signal distribution in the mice, and the results were analyzed with Bruker Molecular imaging software.

In Vivo Antitumor Therapy

A total of 35 mice with tumors measuring approximately 100 mm^3 were chosen and then divided into seven groups, each consisting of 5 mice selected randomly. The specific groups were: (1) NS group, (2) NS+US group, (3) Free Ce6+US group, (4) Au/PB-HA+US group, (5) PB-Ce6-HA+US group, (6) Au/PB-Ce6+US group, and (7) Au/PB-Ce6-HA+US group. Each group of mice was injected with 200 μL of samples (using the Ce6 concentration as the reference concentration, Ce6: 5 $mg{\cdot}kg^{-1}$) every other day through the tail vein. Four hours after the administration, the ultrasonic coupling agent was applied to the tumor sites of the groups with US intervention, and the ultrasonic therapeutic apparatus was used for treatment (1 MHz, 1 $W{\cdot}cm^{-2}$, 5 min). Mice were weighed every day and tumor sizes were measured before administration. Tumor volumes were calculated using the following equation: $V = W^2 \times L/2$, where W and L are the shortest and longest diameters of tumors, respectively. Relative tumor volume was defined as V/V_0 (V_0 is the tumor volume when the treatment was initiated). After mice were sacrificed, H&E staining was carried out.

Statistical Analysis

All statistical evaluations were conducted using the GraphPad Prism software. The data underwent statistical examination utilizing Student's *t*-test and the analysis of variance (ANOVA). Statistical significance is indicated as *($P < 0.05$), **($P < 0.01$), ***($P < 0.001$) and ****($P < 0.0001$).

Results and Discussion

Construction and Characterization of Au/PB-Ce6-HA NPs

PBNPs were prepared by a simple hydrothermal method to induce crystal growth. Here, PVP, as a stabilizer coating on the surface of nanoparticles, can effectively prevent the growth of crystal nuclei and achieve the purpose of controlling particle size. Monodisperse nanoparticles with diameters of about 50 nm were observed in transmission electron microscopy (TEM) images (Figure 1A). Au/PB NPs were further prepared based on PBNPs by directly reducing $HAuCl_4$ in water using sodium borohydride. As shown in Figure 1B, small black spots with a diameter of around 4 nm were observed on the outer surface of PBNPs, indicating the formation of AuNPs. As illustrated in Figure S1, the hydrodynamic diameter of pristine PBNPs was 107.7 ± 3.5 nm, with a zeta potential of −15.0 ± 1.2 mV (Figure 1D). After deposition of AuNPs, the Au/PB NPs exhibited a marginally increased diameter of 111.9 ± 2.7 nm (Figure S1) and a slightly attenuated negative charge of −12.7 ± 1.5 mV (Figure 1D). Upon loading Ce6 into the porous framework of Au/PB NPs, the resultant Au/PB-Ce6 complex maintained a comparable hydrodynamic size (120.8 ± 4.3 nm, Figure S1), indicating minimal steric impact from the encapsulated small-molecule sonosensitizer. Notably, the zeta potential shifted significantly to −25.9 ± 1.1 mV (Figure 1D), attributable to the intrinsic negative charge of Ce6. Further modification with thiolated hyaluronic acid (HA-SH) via Au-S bonding yielded Au/PB-Ce6-HA nanoparticles. This surface engineering induced a substantial increase in hydrodynamic diameter to 160.1 ± 3.2 nm (Figure S1) and amplified the zeta potential to −32.7 ± 1.3 mV (Figure 1D). The enhanced negative surface charge confers two critical advantages: (1) it strengthens interparticle electrostatic repulsion, ensuring colloidal stability in aqueous media; (2) it minimizes nonspecific protein adsorption in blood circulation through charge repulsion with anionic plasma proteins, thereby promoting tumor-targeted drug delivery.

An Ultraviolet-visible (UV-Vis) spectrophotometer (UV-2700, Shimadzu, Japan) was employed to perform scanning on PBNPs, Au/PB NPs, and AuNPs within the wavelength range of 300–800 nm. As depicted in Figure 1E, the absorption spectrum of PBNPs exhibited a peak at approximately 680 nm, which can be attributed to the charge transfer occurring between Fe^{2+} and Fe^{3+} within PBNPs. The prepared AuNPs with small particle sizes showed a typical localized surface plasmon resonance (LSPR) peak at 507 nm. Further porosity analysis validated the mesoporous structure essential for drug loading. According to the IUPAC 2015 classification, the nitrogen adsorption-desorption

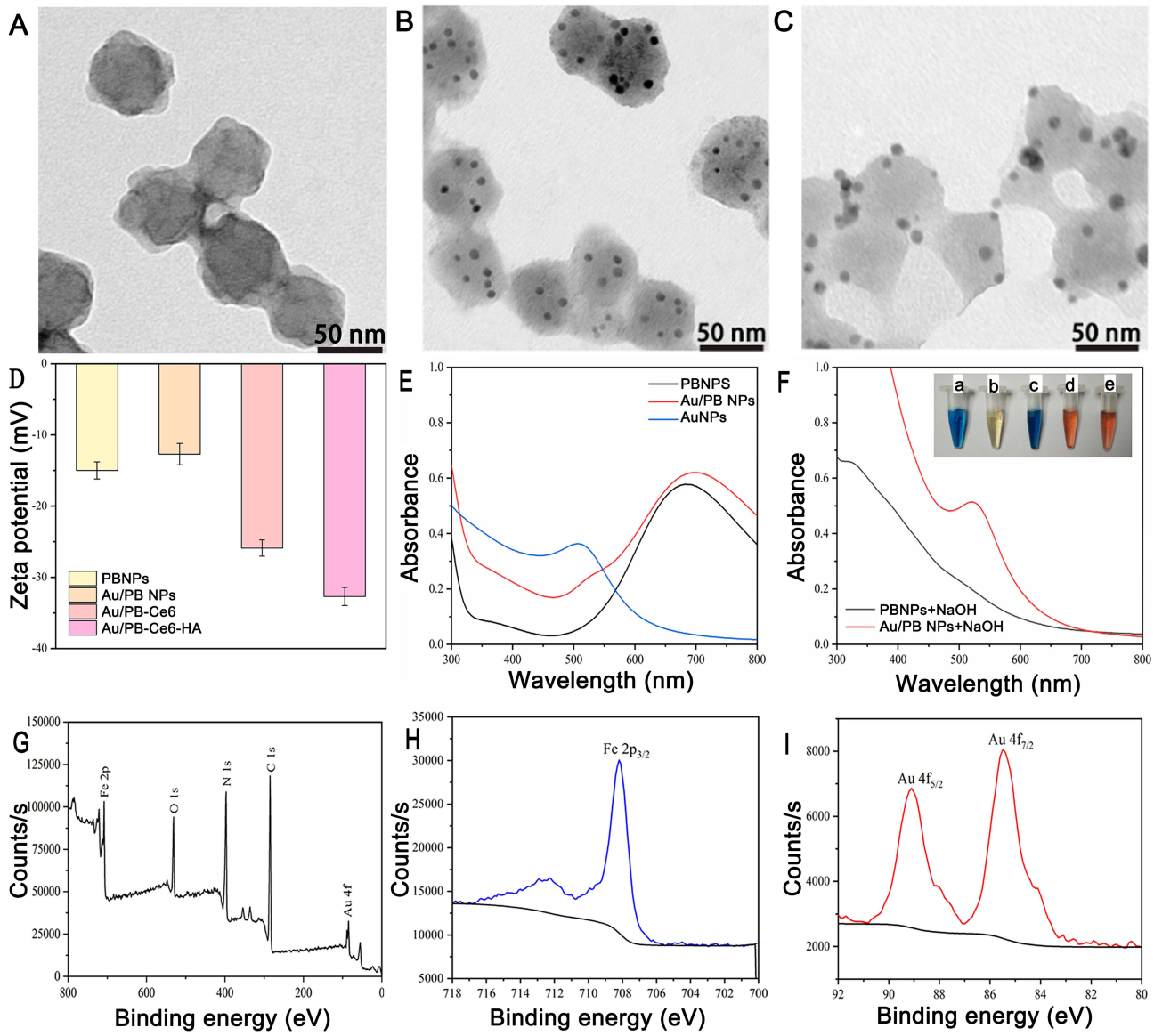

Figure 1 Characterization of Au/PB-Ce6-HA NPs. TEM images of PBNPs (**A**), Au/PB NPs (**B**) and Au/PB-Ce6-HA (**C**). (**D**) Zeta potentials of PBNPs, Au/PB NPs, Au/PB-Ce6, Au/PB-Ce6-HA. (**E**) UV-Vis absorption spectra of PBNPs, Au/PB NPs, and AuNPs. (**F**) UV-Vis absorption spectra of PBNPs and Au/PB NPs after reacting with NaOH solution, respectively. Inset: From left to right are the color change diagrams of (a) PBNPs, (b) PBNPs+NaOH, (c) Au/PB NPs, (d) Au/PB NPs+NaOH, and (e) AuNPs. (**G**) The XPS spectra of Au/PB NPs. (**H**) and (**I**) The XPS characteristic spectra of Fe 2p and Au 4f, respectively.

isotherm of PB NPs exhibited a Type IV curve characteristic of mesoporous materials (Figure S2A). The observed H3-type hysteresis loop, arising from non-coincident adsorption-desorption branches, indicates slit-shaped pores formed by nanoparticle stacking during lattice assembly and post-drying aggregation. BET measurements revealed a specific surface area of 1.12 m^2/g (potentially underestimated due to particle agglomeration), while BJH pore size distribution showed a primary peak at 1.91 nm with secondary maxima at 3.21, 5.65, and 9.62 nm (Figure S2B). This multimodal distribution reflects heterogeneous pore structures comprising intrinsic cavities and interparticle voids, collectively enabling efficient drug encapsulation. In comparison to PBNPs, Au/PB NPs exhibited an enhanced absorption peak within the range of 500–550 nm, which can be attributed to the deposition of AuNPs onto the surface of PBNPs, thereby validating the integration of the absorption peaks of PBNPs and AuNPs in the Au/PB NPs. PBNPs degraded gradually under strong alkaline conditions, and the solution changed from blue to pale yellow due to the combination of OH^- in the solution and the generated Fe^{3+} to form iron hydroxide. Therefore, to further confirm the successful loading of AuNPs on PBNPs, the same concentration of PBNPs and Au/PB NPs were reacted with a sodium hydroxide (NaOH) solution (1 $mol \cdot L^{-1}$),

respectively. As shown in Figure 1F, due to the gradual decomposition of PBNPs, the characteristic absorption peak in the range of 600–800 nm disappeared. Along with the reaction of Au/PB NPs with NaOH solution, an absorption peak emerged near 520 nm, which was consistent with the typical LSPR peak of AuNPs with small particle sizes, indicating the existence of AuNPs in the solution after the decomposition of PBNPs in Au/PB NPs. In addition, as shown in Figure 1E and F, after the reaction of Au/PB NPs with NaOH solution, the blue color of the solution weakened to the same orange-red color as that of the small-sized AuNPs solution, whereas the PBNPs solution turned into a transparent light yellow color. These findings collectively confirmed the successful loading of AuNPs on PBNPs.

X-ray photoelectron spectroscopy (XPS) was employed to authenticate the existence of each element (C, N, Fe, Au, O) within Au/PB NPs, providing direct evidence for the successful fabrication of the hybrid nanomaterials (Figure 1G). Comparing the characteristic spectra of Fe 2p and Au 4f with the standard spectra, it can be seen that the valence of Fe element was +2 and +3, and the valence of Au was 0, indicating that the deposited AuNPs were elemental gold (Figure 1H and I).

The coexistence of specific absorptions corresponding to Ce6 and Au/PB NPs was confirmed through UV-Vis spectroscopy (Figures 1E and 2A). The sonosensitizer Ce6 was effectively encapsulated within the porous Au/PB NPs, with a loading efficiency of 116 $mg{\cdot}g^{-1}$. This can be attributed to the porous structure and significant specific surface area of Au/PB NPs, enabling the efficient absorption and storage of drug molecules. Drug encapsulation did not significantly change the size of the hybrid nanoparticles, as demonstrated by dynamic light scattering (DLS) measurements (Figure S1, Supplementary Materials).

To enhance colloidal stability, regulate catalytic activity, and promote tumor-targeted accumulation, Au/PB NPs were modified with thiolated hyaluronic acid (HA-SH) through Au-S bonding. This conjugate was synthesized via a validated two-step process (Figure S3), with comprehensive NMR characterization confirming structural fidelity: the persistent acetyl methyl signal at ~ δ 1.94 ppm across all derivatives (Figures S4–S6) demonstrated preserved HA backbone architecture essential for biological recognition; newly emerged methylene protons at δ 2.60 ppm in HA-SH (Figure S6) verified free thiol formation; and characteristic peak broadening at δ 3.50 ppm indicated thiol stabilization through hydrogen bonding networks. Quantitative analysis (Figures 2B and C) determined a 21.5% thiol grafting rate. The engineered interface confers synergistic advantages including steric-electrostatic stabilization evidenced by consistent hydrodynamic size (Figure S1) and enhanced negative zeta potential (Figure 1D). This multifunctional modification simultaneously addresses colloidal stability in physiological environments, prevention of off-target catalytic effects, and receptor-mediated tumor accumulation, collectively fulfilling critical requirements for therapeutic efficacy.

In addition, HA-SH-modified nanoparticles were characterized by TEM and DLS (Figure 1C and Figure S1, Supplementary Materials). It can be seen that the average hydrodynamic diameter of the modified nanoparticles was increased around 39 nm, and that the zeta potential of Au/PB-Ce6-HA was around −32.7 mV (Figure 1D), which is beneficial for prolonging the circulation time.

Establishment of Ce6 Quantification Method

Determination of Optimal Detection Wavelength

UV-Vis spectral scanning of Ce6 solutions (300–800 nm range, Figure S7) revealed two distinct absorption peaks at 404 nm and 641 nm, with significantly higher intensity observed at 404 nm. Prussian blue nanocarriers exhibited strong absorption between 600–800 nm, causing substantial spectral interference at 641 nm. Consequently, 404 nm was selected as the detection wavelength to ensure accurate Ce6 quantification free from nanocarrier interference.

Calibration Curve Construction

A linear calibration curve was established by plotting Ce6 concentration against absorbance at 404 nm (Figure S8). The regression equation was determined as:

$$y = 0.0936x + 0.043 \left(R^2 = 0.9997\right)$$

where y represents absorbance and x denotes Ce6 concentration ($\mu g{\cdot}mL^{-1}$). The excellent linearity ($R^2 > 0.999$) across 1–10 $\mu g{\cdot}mL^{-1}$ satisfies quantitative analysis requirements for precise drug content determination in nanoparticle formulations.

https://doi.org/10.2147/IJN.S490343

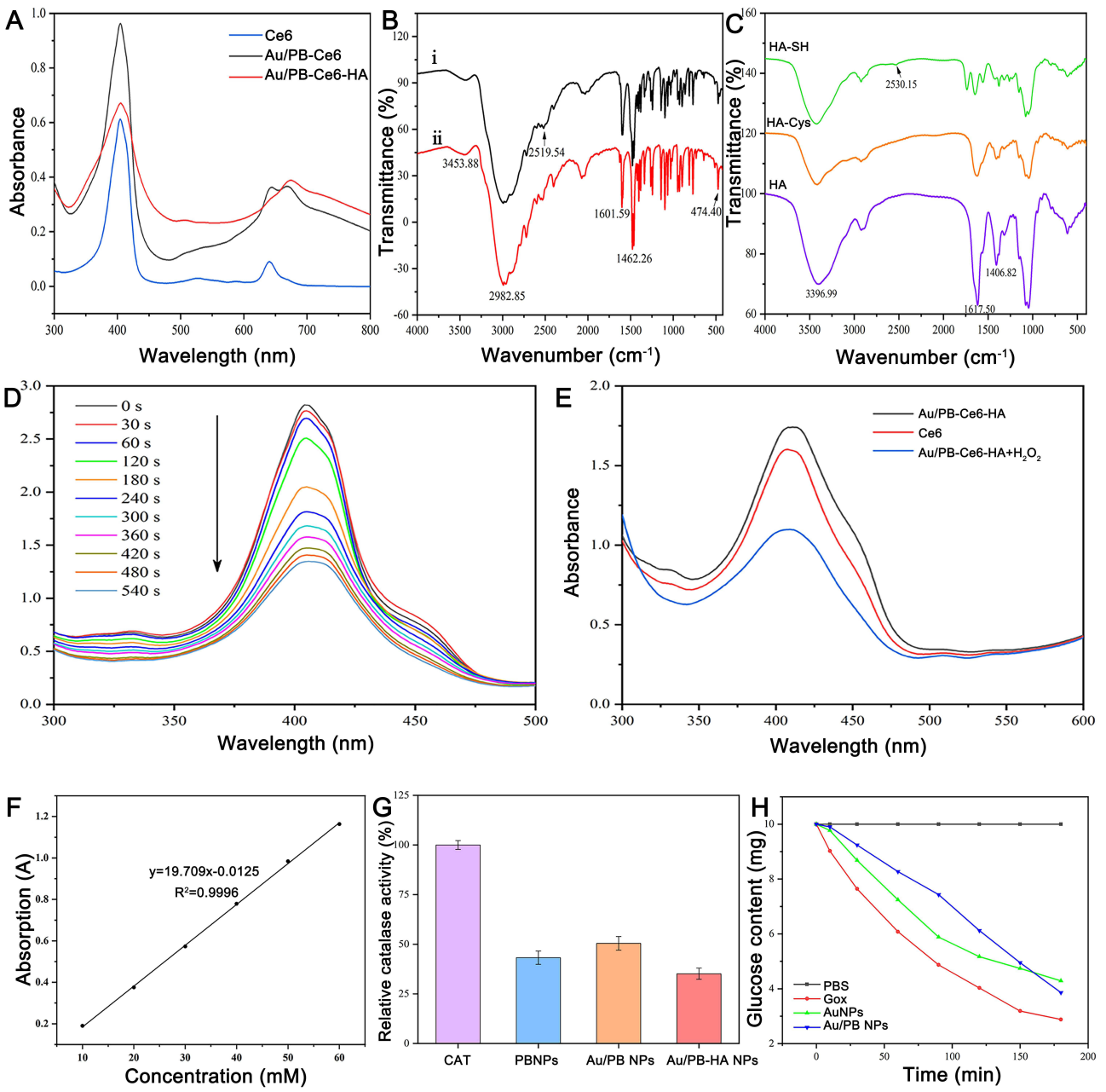

Figure 2 Characterization of HA-SH and investigation of catalytic activity of nanoparticles. **(A)** UV-Vis absorption spectra of Ce6, Au/PB-Ce6 and Au/PB-Ce6-HA. (**B**) The FT-IR spectra of (i) cysteamine and (ii) cystamine. (**C**) The FT-IR spectra of HA, HA-Cys and HA-SH. (**D**) UV-Vis absorption spectra of DPBF added into free Ce6 solution under different durations of ultrasonic irradiation. (**E**) UV-Vis absorption of DPBF in solutions of free Ce6, Au/PB-Ce6-HA and Au/PB-Ce6-HA+H_2O_2 with the same Ce6 concentration after US treatment (1 MHz, 1 W·cm^{-2}) for 4min. (**F**) Standard curve of H_2O_2 absorbance at 240 nm. (**G**) Relative catalase-like activity for the interactions of PBNPs, Au/PB NPs and Au/PB-HA NPs with H_2O_2, respectively (n = 3). (**H**) Glucose oxidase-like activity of GOx, AuNPs and Au/PB NPs.

Drug Release Behavior Assessment

Systematic release studies using Ce6 as a model drug confirmed the dual-responsive mechanism mediated by acidic pH and hyaluronidase. Under physiological conditions (pH 7.4), minimal drug release (6.6%) occurred after 12 h (Figure S9a). Conversely, acidic environments significantly accelerated release: 9.3% at tumor-mimetic pH 5.5 and 22.8% under lysosomal pH 4.5 (Figure S9b,c). The most enhancement emerged with hyaluronidase co-treatment (150 U·mL^{-1}, pH 4.5), where burst release reached 62.92% within 12 h (Figure S9d). This synergistic acceleration stems from complementary mechanisms: acid-induced protonation of CN^- bridges weakens Fe-CN-Fe coordination, while enzymatic degradation of the hyaluronic acid coating exposes Prussian blue nanopores. Consequently, spatiotemporally controlled

release is achieved—suppressing systemic leakage during circulation (neutral pH) yet enabling intracellular drug eruption in tumor lysosomes (acidic/enzyme-rich milieu)—thus enhancing therapeutic efficacy while minimizing toxicity.

Detection of the Ability to Generate $^1O_2$

Next, we assessed the capacity of free sonosensitizer Ce6 and Au/PB-Ce6-HA to generate $^1O_2$ employing a UV-Vis spectrophotometer (UV-2700, Shimadzu, Japan) with DPBF as the fluorescent probe. As shown in Figure 2D, under the influence of ultrasonic irradiation, the absorbance of DPBF in the solution with free Ce6 decreased gradually, indicating the generation of $^1O_2$. From Figure 2E, it can be seen that when Au/PB-Ce6-HA or free Ce6 solutions with the same concentration of Ce6 were exposed to US for the same time, Au/PB-Ce6-HA generated less $^1O_2$ than free Ce6 due to the encapsulation of nanoparticles. However, after H_2O_2 was added, the $^1O_2$ yield of Au/PB-Ce6-HA increased significantly compared to free Ce6, which was due to the reaction of PBNPs in Au/PB-Ce6-HA with H_2O_2 to produce O_2.

Detection of Catalase-Like Activity

The absorption wavelength of H_2O_2 is approximately 240 nm. We detected the changes in absorbance at 240 nm employing a UV-Vis spectrophotometer after the reaction of PBNPs, Au/PB NPs, Au/PB-HA and CAT with the same concentration of H_2O_2 (60 mM) for 2 h. Then the relative catalase-like activity indicating their catalytic performance was calculated (Figure 2F and G). The results showed that the modification of HA had little effect on the CAT-like activity of Au/PB NPs.

Detection of Oxidase-Like Activity

The glucose oxidase-like activities of AuNPs and Au/PB NPs were then investigated. As shown in Figure 2H, AuNPs with small particle sizes showed high catalytic activity in the first 90 min due to their large specific surface area and high catalytic activity, but as AuNPs gathered, the catalytic activity gradually disappeared. Compared to AuNPs, Au/PB NPs demonstrated a slower catalytic reaction rate within the initial few minutes. However, the reaction speed was accelerated over time, which could be attributed to the fact that the AuNPs deposited on PBNPs initially transformed glucose into gluconic acid and H_2O_2, and H_2O_2 was then decomposed by the PBNPs to yield O_2. In the presence of O_2, AuNPs could accelerate the oxidation of glucose. In addition, the deposition of AuNPs on PBNPs alleviated aggregation, which helped to maintain the glucose oxidase-like activity of Au/PBNPs. In conclusion, while isolated AuNPs show faster initial kinetics, their rapid aggregation limits therapeutic utility. Integrating AuNPs onto PBNPs sacrifices transient speed for sustained, tumor-targeted cascade reactions.

Cell Viability

The cytotoxicity of nanoparticles on HepG2 cells was assessed using the MTT assay. As shown in Figure 3A, PBNPs, Au/PB NPs, and Au/PB-HA exhibited high safety and compatibility after co-incubation with cells for 24 h at a concentration of up to 100 $\mu g \cdot mL^{-1}$. Hence, they could be used for the subsequent in vitro and in vivo experiments.

The cytotoxicity of Ce6 and Au/PB-Ce6-HA on HepG2 cells was investigated in the presence and absence of ultrasonic irradiation (Figure 3B). It was shown that in the absence of ultrasonic irradiation, Ce6 and Au/PB-Ce6-HA did not significantly inhibit the proliferation of HepG2 cells with the increase of concentration, while cell viability remained above 80% at a concentration below 100 $\mu g \cdot mL^{-1}$, indicating that Ce6 and nano-carriers without ultrasonic irradiation had little cytotoxicity to cells. For sonodynamic therapy alone (Ce6+US), the cell viability gradually decreased with the increase in drug concentration, although the treatment effect was insignificant. In contrast, the survival rate of the Au/PB-Ce6-HA+US group was only 18.47% at 100 $\mu g \cdot mL^{-1}$. The modification of the nanoformulation with HA endowed it with active targeting ability, which ensured that it could reach a higher concentration at the target site. AuNPs and PBNPs with nanozyme activity can realize cascade catalytic reactions, consume glucose and release oxygen, alleviate the hypoxic environment, provide the raw material for SDT, and play a synergistic effect in causing massive death of HepG2 cells. AuNPs and PBNPs, which exhibit nanozyme activities, could facilitate cascade catalytic reactions. These reactions alleviated hypoxia by consuming glucose and releasing oxygen, providing the necessary materials for SDT. Their synergistic effects resulted in a substantial death of HepG2 cells.

 https://doi.org/10.2147/IJN.S490343

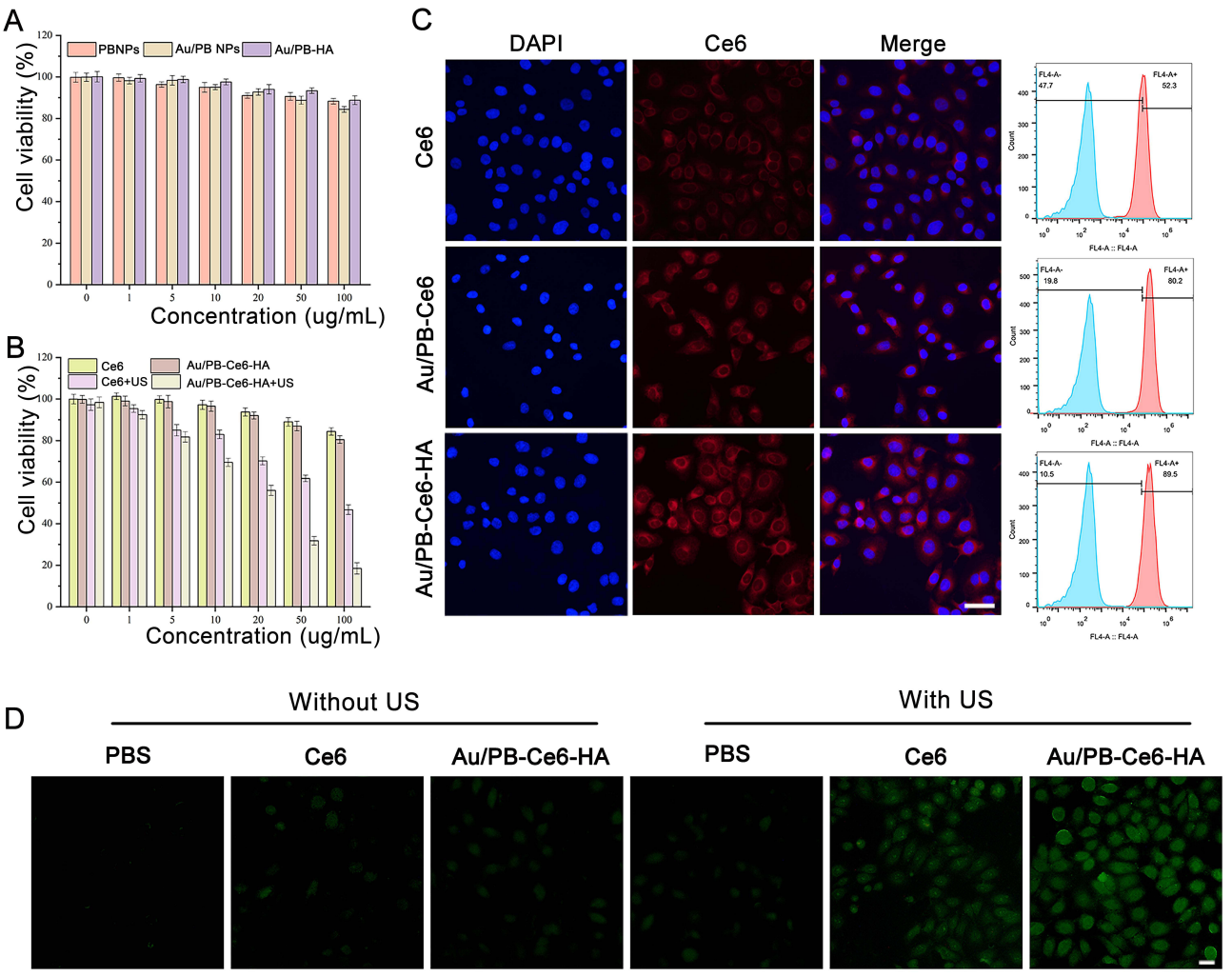

Figure 3 In vitro evaluation of tumor therapeutic effect of Au/PB-Ce6-HA nanocatalytic platform. (**A**) Cell viability of nanocarriers incubated with HepG2 cells for 24 h (n = 6). (**B**) The viability of HepG2 cells incubated with different concentrations of Ce6 and Au/PB-Ce6-HA for 24 h in the presence or absence of US, were assessed. The US condition was 1 MHz, 1.0 W cm^{-2}, 1 min (n = 6). (**C**) The uptake of different drug administration groups in HepG2 cells after 4 h of incubation (scale bar = 50 μm). (**D**) Under a fluorescent microscope, the green fluorescence was observed to examine intracellular ROS formation in HepG2 cells incubated with Ce6 and Au/PB-Ce6-HA for 4 h, with or without ultrasound irradiation, respectively (scale bar = 20 μm). The Ce6 concentration was 10 μg mL^{-1}, and the US conditions were 1 MHz, 1.0 W cm^{-2}, 1 min.

Cellular Uptake

Cellular uptake of the nanoparticles was investigated using Ce6, a sonosensitizer that exhibits red fluorescence. Free Ce6, Au/PB-Ce6, and Au/PB-Ce6-HA were incubated with HepG2 cells, respectively. It was found that the fluorescence intensity of Ce6 gradually increased with incubation time and was mainly observed in the cytoplasm rather than in the nucleus (Figure S10, Supplementary Materials). In addition, the results of fluorescence microscopy and flow cytometry showed that after incubation with HepG2 cells for 4 h, the Au/PB-Ce6-HA group showed an obvious red fluorescence signal, indicating that Au/PB-Ce6-HA could be effectively internalized by cells (Figure 3C). This uptake ensures the subsequent efficient intracellular cascade nanocatalytic reactions, leading to the eradication of cancer cells.

In Vitro Intracellular ROS Detection

ROS has been proven to play a crucial part in SDT-induced cellular death, and the therapeutic effect of SDT can be verified by measuring the level of intracellular ROS. ROS fluorescent probe, DCFH-DA, is a non-fluorescent cell-permeable compound that, upon de-esterification, can be transformed into 2′,7′-dichlorofluorescein (DCF) which exhibits intense green fluorescence. Therefore, intracellular ROS generated can be quantified by measuring the fluorescence

intensity. As expected, blank HepG2 cells treated with PBS showed negligible fluorescence both before and after ultrasound treatment, indicating that ultrasonic stimulation alone had little effect on ROS production in tumor cells. In contrast, cells incubated with free Ce6 and Au/PB-Ce6-HA NPs, respectively, showed significantly enhanced green fluorescence after ultrasound irradiation, indicating that the level of ROS increased, and Ce6 played the role of sonosensitizer in sonodynamic therapy. The Au/PB NPs effectively elevated intracellular ROS levels through ultrasonic irradiation, indirectly highlighting the importance of O_2 for SDT (Figure 3D). As shown in Figure S11, semi-quantitative analysis of intracellular ROS revealed Au/PB-Ce6-HA+US generated around 60.27 a.u. fluorescence intensity - significantly exceeding free Ce6+US (around 41.56 a.u.) and demonstrating 12.7-fold enhancement over PBS controls. This 45% improvement confirms the nanocomposite's superior ability to overcome hypoxia through synergistic nanozyme activity. Notably, ultrasound alone induced measurable ROS (PBS+US: around 12.04 a.u.), while the unirradiated nanocomposite showed 44% higher cellular accumulation than free Ce6, validating both enhanced targeting and catalytic ROS amplification.

Tumor Uptake of Au/PB-Ce6-HA in Vivo

The in vivo antitumor activity of Au/PB-Ce6-HA under US irradiation was evaluated in the H22 tumor-bearing mice model, following the treatment procedure shown in Figure 4A. The biodistribution of nanoformulations in mice within 24 hours after injection was first assessed by in vivo fluorescence imaging (Figure 4B). After intravenous administration, the formulations of each group were rapidly distributed in various tissues of mice. The fluorescence intensity of the tumor site in the Ce6 group reached the maximum at 4 h, then gradually eliminated at a faster rate. At 24 h, little fluorescence was observed at the tumor site. However, Au/PB-Ce6 and Au/PB-Ce6-HA groups maintained strong fluorescence in the tumor tissue. The Au/PB-Ce6-HA group demonstrated a significant enhancement in drug accumulation at the tumor site compared to the free Ce6 group. Considering the distribution of drugs in vivo, 4 h after administration was determined as the optimal treatment time for SDT.

Antitumor Effect of Au/PB-Ce6-HA in Vivo

Encouraged by the high efficiency, prolonged blood circulation and significant tumor aggregation effect of extracellular nanocatalytic therapy in killing cancer cells, we evaluated the in vivo nanocatalytic therapeutic efficiency of Au/PB-Ce6-HA on H22 tumor-bearing mice. Throughout the 15-day duration of the treatment, there was no notable disparity in the body weight of mice between the treatment and control groups (Figure 4C). At the therapeutic endpoint, mice were euthanized and representative tumor tissues were excised and photographed (Figure S12). The relative tumor volumes of tumor-bearing mice in the normal saline (NS) group and NS+US group continued to increase rapidly with time. In addition, there was no notable distinction between the two groups, indicating that US alone had no obvious inhibitory effect on tumor growth. The Ce6+US group (ie, the SDT group) did not exhibit optimal effectiveness in tumor suppression, possibly due to Ce6's high metabolic rate and insufficient O_2 content within the tumor tissues. In contrast, the Au/PB-Ce6-HA nanocomposites combined with US group, demonstrated significant efficacy in inhibiting tumor growth. The tumor weight and volume showed a significant downward trend 7 days after administration (Figure 4D and E). Hematoxylin and eosin (H&E) staining indicated that the formulation of Au/PB-Ce6-HA resulted in the highest level of apoptotic and necrotic cells in tumor tissues (Figure 5A). The CD44-directed targeting strategy intrinsically enhances tumor specificity, reducing normal cell exposure. Future studies will include normal hepatocyte controls to comprehensively assess safety windows.

Biosafety of Au/PB-Ce6-HA

The biosafety of nano-carriers was carefully evaluated before the antitumor studies were conducted. As shown in Figure 5B, treatment with different concentrations of Au/PB-HA NPs did not cause obvious hemolysis within the test concentration range. Furthermore, to evaluate the in vivo biocompatibility of the nanoplatform, H&E staining of tissue sections of main organs was analyzed. Following a 14-day course of treatment, the treatment group of mice exhibited no

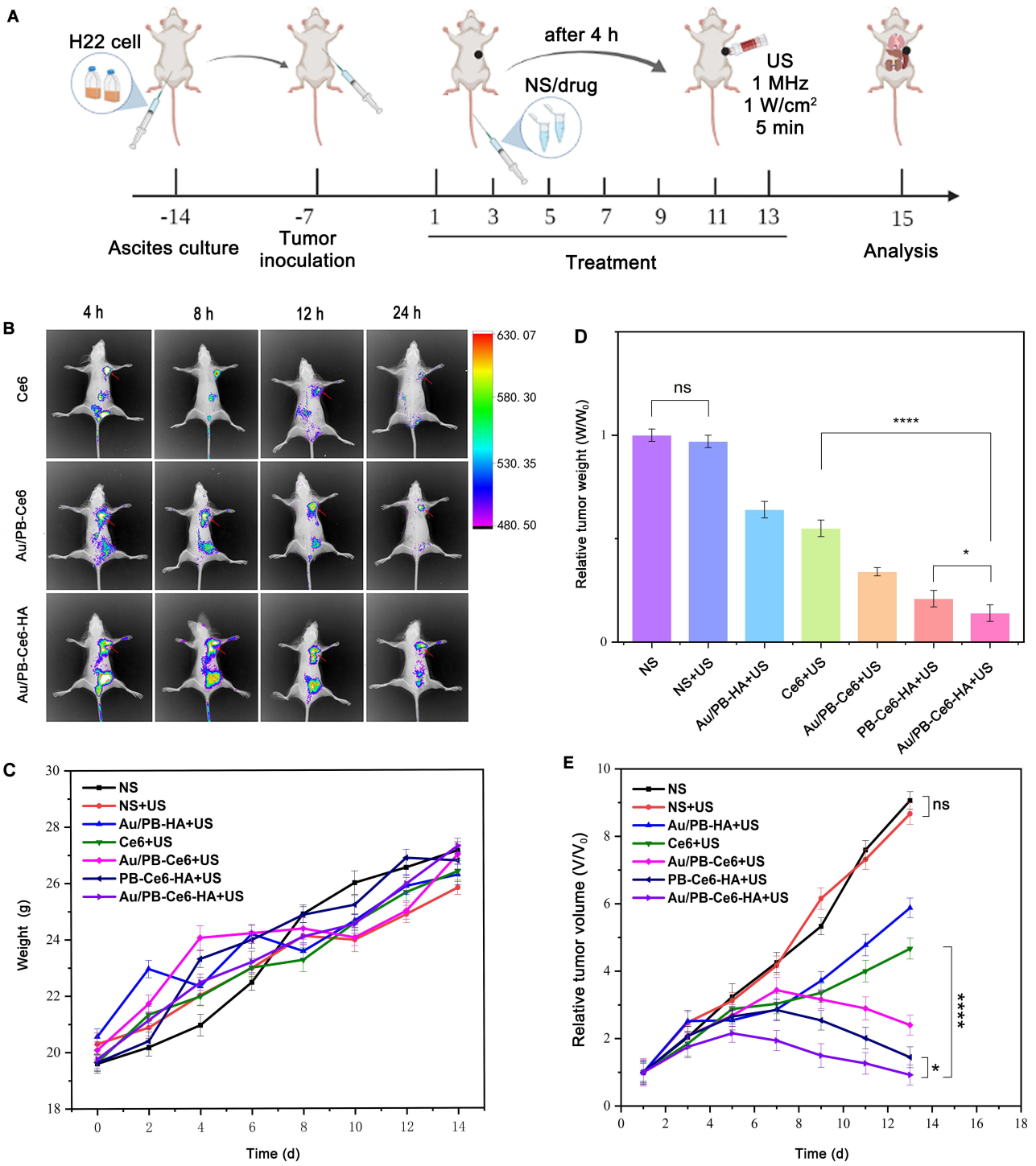

Figure 4 In vivo evaluation of tumor therapeutic efficacy of Au/PB-Ce6-HA nanocatalytic platform. (**A**) Schematic illustration and administration schedule for the mice model. (**B**) In vivo distribution of Ce6, Au/PB-Ce6, and Au/PB-Ce6-HA in tumor-bearing mice models at different time points. (**C**) Changes in weight of H22 tumor-bearing mice with different treatment groups over time. (**D**) Relative tumor weight of mice in different treatment groups. (**E**) Relative tumor volume changes with time of H22 tumor-bearing mice with diverse treatment groups (n = 5).

apparent pathological adverse reactions in their main organs compared to the NS group (Figure 5C). These findings suggest that Au/PB-Ce6-HA, functioning as a nanocatalyst, demonstrates good biocompatibility and serves as a safe biotherapeutic agent.

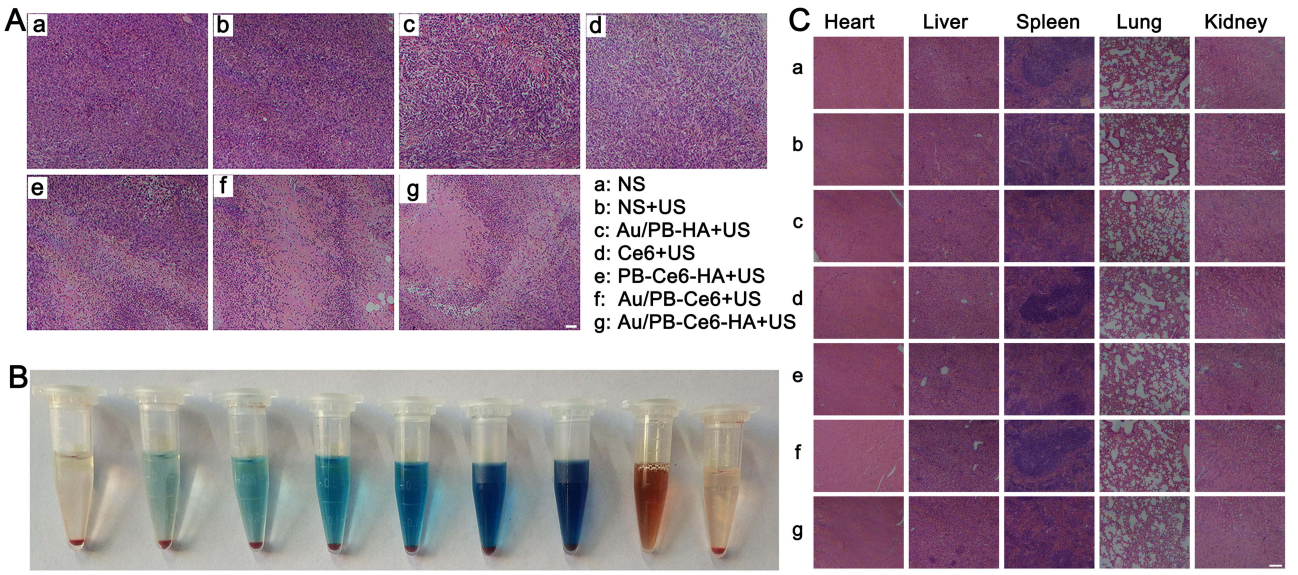

Figure 5 Investigation of the in vivo anti-tumor activity and biosafety of nanoparticles. (**A**) Tumor sections stained with H&E after different treatments (scale bar = 25 μm). (**B**) Hemolysis test. Arranged in order from left to right are normal saline, 10 μg/mL, 50 μg/mL, 100 μg/mL, 200 μg/mL, 500 μg/mL and 1000 μg/mL of Au/PB-HA NPs, followed by water and PBS. (**C**) H&E staining of key organ sections following various treatments (scale bar = 200 μm).

Conclusion

In summary, an intelligent composite nanomaterial was successfully developed employing gold nanoparticles with glucose oxidase-like activity and Prussian blue nanoparticles with catalase-like activity for the combined therapy of sonodynamic and starvation treatments against tumors. Specifically, gold nanoparticles were in situ grown on Prussian blue nanoparticles capable of loading the sonosensitizer Chlorin e6, resulting in Au/PB composite nanoparticles. With thiolated hyaluronic acid as the capping and targeting agent, Au/PB composite nanocarriers were modified through gold-sulfur bonds, ensuring the stability of the nanoparticles, significantly increasing their accumulation in tumor sites, enhancing their antitumor performance, and reducing toxic side effects. Interestingly, gold nanoparticles can oxidize intracellular glucose to produce gluconic acid and hydrogen peroxide for starvation therapy of tumors. Prussian blue nanoparticles not only serve as carriers for sonosensitizers but also catalyze the production of oxygen from endogenous and exogenous hydrogen peroxide. Under ultrasonic irradiation, the sonosensitizer further utilizes oxygen to generate highly toxic ROS for sonodynamic therapy of tumors. Both in vitro and in vivo studies demonstrate that the combination of starvation therapy and sonodynamic therapy exhibits excellent synergy in effectively inhibiting tumor growth.

This work addresses two critical barriers in HCC therapy: (1) hypoxia-induced resistance to energy-dependent treatments, and (2) untargeted exploitation of metabolic vulnerabilities. The Au/PB-Ce6-HA platform enables self-sustaining therapeutic cascades within tumors—converting endogenous glucose into cytotoxic ROS under ultrasound—providing a minimally invasive solution for inoperable HCC.

Following this proof-of-concept study, we recommend three strategic research directions: 1. Improve toxicity profiling by using ^{64}Cu-labeled PET to measure nanoparticle pharmacokinetics and clearance rates. 2. Develop orthotopic HCC models using contrast-enhanced ultrasound for real-time monitoring of treatments. 3. Utilize nanozyme-induced immunogenic cell death markers to stimulate $CD8^+$ T-cells through anti-PD1 checkpoint inhibition in combinatorial immunotherapy. We believe these efforts will bridge translational gaps toward clinical applications.

Abbreviations

PDT, photodynamic therapy; SDT, sonodynamic therapy; H_2O_2, hydrogen peroxide; PBNPs, Prussian blue nanoparticles; AuNPs, gold nanoparticles; Ce6, chlorin e6; HA-SH, thiolated hyaluronic acid; PTT, photothermal therapy; NIR, near-infrared; O_2, oxygen; ROS, reactive oxygen species; $^1O_2$, singlet oxygen; •OH, hydroxyl radicals; US, ultrasound; HIFU, high intensity focused ultrasound; TME, tumor microenvironment; EPR, enhanced permeability and retention; GOx,

https://doi.org/10.2147/IJN.S490343

glucose oxidase; CAT, catalase; TEM, transmission electron microscopy; UV-Vis, ultraviolet-visible; LSPR, localized surface plasmon resonance; NaOH, sodium hydroxide; XPS, X-ray photoelectron spectroscopy; DLS, dynamic light scattering; DPBF, 1,3-diphenylisobenzofuran; DCFH-DA, 2′,7′-dichlorodihydrofluorescein diacetate; DCF, 2′,7′-dichlorofluorescein; NS, normal saline; H&E, hematoxylin and eosin; $K_3[Fe(CN)_6]$, Potassium ferricyanide; HA, hyaluronic acid; PVP, polyvinylpyrrolidone; $NaBH_4$, sodium borohydride; DAPI, 4′,6-Diamidino-2-phenylindole; MTT, 3-(4,5-Dimethylthiazol-2-yl)-2,5-diphenyltetrazolium bromide; OD, optical density; GOx, glucose oxidase; FBS, fetal bovine serum; CLSM, confocal laser scanning microscopy.

Funding

This work was supported by the National Natural Science Foundation of China (No. 82003298), the Natural Science Foundation of Chongqing (No. cstc2019jcyj-msxmX0035), the Scientific Research Seedling Project of Chongqing Medicinal Biotechnology Association (No. cmba2022kyym-zkxmQ0009), the Scientific and Technological Project of Henan Province (No. 232102310392), the Key Scientific Research Projects of Colleges and Universities in Henan Province (25A360021), the Key Research Projects of Henan Higher Education Institutions (No. 18A350003), the Natural Science Foundation of Henan Province (No. 162300410044) and the Chongqing Clinical Pharmacy Key Specialties Construction Project.

Disclosure

The authors report no conflicts of interest in this work.

References

1. Shin HS, Jun BG, Yi S. Impact of diabetes, obesity, and dyslipidemia on the risk of hepatocellular carcinoma in patients with chronic liver diseases. *Clin Mol Hepatol*. 2022;28(4):773–789. doi:10.3350/cmh.2021.0383
2. Li C, Xu X. Biological functions and clinical applications of exosomal non-coding RNAs in hepatocellular carcinoma. *Cell Mol Life Sci*. 2019;76(21):4203–4219. doi:10.1007/s00018-019-03215-0
3. Yang M, Mu Y, Yu X, et al. Survival strategies: How tumor hypoxia microenvironment orchestrates angiogenesis. *Biomed Pharmacother*. 2024;176:116783. doi:10.1016/j.biopha.2024.116783
4. Zhang L, Xu J, Zhou S, et al. Endothelial DGKG promotes tumor angiogenesis and immune evasion in hepatocellular carcinoma. *J Hepatol*. 2024;80(1):82–98. doi:10.1016/j.jhep.2023.10.006
5. Xia P, Zhang H, Lu H, et al. METTL5 stabilizes c-Myc by facilitating USP5 translation to reprogram glucose metabolism and promote hepatocellular carcinoma progression. *Cancer Commun*. 2023;43(3):338–364. doi:10.1002/cac2.12403
6. Xu M, Yang L, Lin Y, et al. Emerging nanobiotechnology for precise theranostics of hepatocellular carcinoma. *J Nanobiotechnol*. 2022;20(1):427. doi:10.1186/s12951-022-01615-2
7. Shirvalilou S, Tavangari Z, Parsaei MH, et al. The future opportunities and remaining challenges in the application of nanoparticle-mediated hyperthermia combined with chemo-radiotherapy in cancer. *WIREs Nanomed Nanobiotechnol*. 2023;15(6):e1922. doi:10.1002/wnan.1922
8. Ouyang J, Xie A, Zhou J, et al. Minimally invasive nanomedicine: nanotechnology in photo-/ultrasound-/radiation-/magnetism-mediated therapy and imaging. *Chem Soc Rev*. 2022;51(12):4996–5041. doi:10.1039/D1CS01148K
9. Wu H, Wang M, Liang L, et al. Nanotechnology for hepatocellular carcinoma: from surveillance, diagnosis to management. *Small*. 2021;17(6):2005236. doi:10.1002/smll.202005236
10. Xiong Y, Rao Y, Hu J, Luo Z, Chen C. Nanoparticle-based photothermal therapy for breast cancer non-invasive treatment. *Adv Mater*. 2023;2305140. doi:10.1002/adma.202305140
11. Cui X, Ruan Q, Zhuo X, et al. Photothermal nanomaterials: a powerful light-to-heat converter. *Chem Rev*. 2023;123(11):6891–6952. doi:10.1021/acs.chemrev.3c00159
12. Liang S, Deng X, Ma P, Cheng Z, Lin J. Recent advances in nanomaterial-assisted combinational sonodynamic cancer therapy. *Adv Mater*. 2020;32(47):2003214. doi:10.1002/adma.202003214
13. Xie J, Wang Y, Choi W, et al. Overcoming barriers in photodynamic therapy harnessing nano-formulation strategies. *Chem Soc Rev*. 2021;50(16):9152–9201. doi:10.1039/d0cs01370f
14. Choi J, Sun I, Sook hwang H, Yeol Yoon H, Kim K. Light-triggered photodynamic nanomedicines for overcoming localized therapeutic efficacy in cancer treatment. *Adv Drug Deliv Rev*. 2022;186:114344. doi:10.1016/j.addr.2022.114344
15. Donohoe C, Senge MO, Arnaut LG, Gomes-da-Silva LC. Cell death in photodynamic therapy: from oxidative stress to anti-tumor immunity. Biochimica et biophysica acta. *Rev Cancer*. 2019;1872(2):188308. doi:10.1016/j.bbcan.2019.07.003
16. Li X, Lovell JF, Yoon J, Chen X. Clinical development and potential of photothermal and photodynamic therapies for cancer. *Nat Rev Clin Oncol*. 2020;17(11):657–674. doi:10.1038/s41571-020-0410-2
17. Guo X, Li L, Jia W, et al. Composite nanomaterials of conjugated polymers and upconversion nanoparticles for NIR-triggered photodynamic/photothermal synergistic cancer therapy. *ACS Appl Mater Interfaces*. 2023. doi:10.1021/acsami.3c12553
18. Wang X, Wu M, Li H, et al. Enhancing penetration ability of semiconducting polymer nanoparticles for sonodynamic therapy of large solid tumor. *Adv Sci*. 2022;9(6):2104125. doi:10.1002/advs.202104125

19. Ashar H, Ranjan A. Immunomodulation and targeted drug delivery with high intensity focused ultrasound (HIFU): principles and mechanisms. *Pharmacol Ther*. 2023;244:108393. doi:10.1016/j.pharmthera.2023.108393
20. Liu T, Zhang N, Wang Z, et al. Endogenous catalytic generation of O(2) bubbles for in situ ultrasound-guided high intensity focused ultrasound ablation. *ACS Nano*. 2017;11(9):9093–9102. doi:10.1021/acsnano.7b03772
21. Zheng Y, Ye J, Li Z, Chen H, Gao Y. Recent progress in sono-photodynamic cancer therapy: from developed new sensitizers to nanotechnology-based efficacy-enhancing strategies. *Acta Pharm Sin B*. 2021;11(8):2197–2219. doi:10.1016/j.apsb.2020.12.016
22. Yang F, Dong J, Li Z, Wang Z. Metal-Organic Frameworks (MOF)-assisted sonodynamic therapy in anticancer applications. *ACS Nano*. 2023;17(5):4102–4133. doi:10.1021/acsnano.2c10251
23. Qian X, Zheng Y, Chen Y. Micro/Nanoparticle-Augmented Sonodynamic Therapy (SDT): breaking the depth shallow of photoactivation. *Adv Mater*. 2016;28(37):8097–8129. doi:10.1002/adma.201602012
24. Son S, Kim JH, Wang X, et al. Multifunctional sonosensitizers in sonodynamic cancer therapy. *Chem Soc Rev*. 2020;49(11):3244–3261. doi:10.1039/C9CS00648F
25. Gong Z, Dai Z. Design and challenges of sonodynamic therapy system for cancer theranostics: from equipment to sensitizers. *Adv Sci*. 2021;8(10):2002178. doi:10.1002/advs.202002178
26. Wen M, Yu N, Wu S, et al. On-demand assembly of polymeric nanoparticles for longer-blood-circulation and disassembly in tumor for boosting sonodynamic therapy. *Bioact Mater*. 2022;18:242–253. doi:10.1016/j.bioactmat.2022.03.009
27. Jiang Q, Qiao B, Lin X, et al. A hydrogen peroxide economizer for on-demand oxygen production-assisted robust sonodynamic immunotherapy. *Theranostics*. 2022;12(1):59–75. doi:10.7150/thno.64862
28. Feng K, Wang Z, Wang S, et al. Elucidating the catalytic mechanism of Prussian blue nanozymes with self-increasing catalytic activity. *Nat Commun*. 2024;15(1):5908. doi:10.1038/s41467-024-50344-7
29. Lee SM, Kim H, Li P, Park HG. A label-free and washing-free method to detect biological thiols on a personal glucose meter utilizing glucose oxidase-mimicking activity of gold nanoparticles. *Biosens Bioelectron*. 2024;250:116019. doi:10.1016/j.bios.2024.116019
30. Sun L, Li Q, Hou M, et al. Light-activatable Chlorin e6 (Ce6)-imbedded erythrocyte membrane vesicles camouflaged Prussian blue nanoparticles for synergistic photothermal and photodynamic therapies of cancer. *Biomater Sci*. 2018;6(11):2881–2895. doi:10.1039/C8BM00812D
31. Luo W, Zhu C, Su S, et al. Self-catalyzed, self-limiting growth of glucose oxidase-mimicking gold nanoparticles. *ACS Nano*. 2010;4(12):7451–7458. doi:10.1021/nn102592h
32. Dong C, Jiang Q, Qian X, et al. A self-assembled carrier-free nanosonosensitizer for photoacoustic imaging-guided synergistic chemo-sonodynamic cancer therapy. *Nanoscale*. 2020;12(9):5587–5600. doi:10.1039/C9NR10735E
33. Liao S, Cai M, Zhu R, et al. Antitumor effect of photodynamic therapy/sonodynamic therapy/sono-photodynamic therapy of chlorin e6 and other applications. *Mol Pharm*. 2023;20(2):875–885. doi:10.1021/acs.molpharmaceut.2c00824
34. Xu D, Wu L, Yao H, Zhao L. Catalase-like nanozymes: classification, catalytic mechanisms, and their applications. *Small*. 2022;18(37):2203400. doi:10.1002/smll.202203400